Acta Materialia 273 (2024) 119982

Contents lists available at ScienceDirect

Acta Materialia

journal homepage: www.elsevier.com/locate/actamat

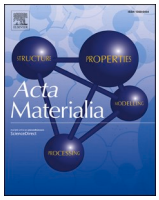

Heterostructure enables anomalous improvement of cryogenic mechanical properties in titanium

Wuli Su [a], Mingsai Wang [a], Fengjiao Guo [a], Hao Ran [a], Qian Cheng [a], Qingyuan Wang [a,b], Yuntian Zhu [c], Xiaolong Ma [c,*], Chongxiang Huang [a,b,*]

[a] School of Aeronautics and Astronautics, Sichuan University, Chengdu, 610065, China
[b] Failure Mechanics and Engineering Disaster Prevention and Mitigation Key Laboratory of Sichuan Province, Sichuan University, Chengdu 610065, Sichuan, China
[c] Department of Materials Science and Engineering, City University of Hong Kong, Hong Kong, China

ARTICLE INFO

Keywords:
Heterostructured materials
Cryogenic mechanical property
Titanium
Hetero-deformation-induced effect
Strain partitioning

ABSTRACT

The pursuit of strong and ductile structures for cryogenic applications has fueled a persistent interest in the microstructure design of metals and alloys. While heterostructure design has recently demonstrated efficacy in achieving superior strength-ductility combinations at room temperature, its potential remains less explored in the cryogenic regime. In this report, we unveil anomalously improved cryogenic mechanical properties of a pure titanium with harmonic heterostructure that matches or even surpasses those of commercial titanium alloys. Through detailed comparison to room-temperature deformation behavior, we reveal that the superior performance of heterostructure at cryogenic temperature is fundamentally underpinned by the amplified inter-zone mechanical incompatibility and the suppression of dislocation cross-slip. The former promotes the generation of abundant geometrically necessary dislocations, and the latter optimally configures them. Collectively, these two factors culminate in the hetero-deformation-induced effect, delivering the anomalous improvement of cryogenic mechanical properties in titanium. These findings not only significantly advance our understanding of cryo-deformation behaviors in heterostructured materials but also offer the potential for developing high-performance materials for cryogenic applications.

1. Introduction

The compelling demand for cryogenic technologies necessitates the development of high-performance materials capable of withstanding substantial stress while maintaining ductility in cryogenic temperatures regime [1,2]. Titanium (Ti) and its alloys have long been investigated as promising materials for cryogenic structures such as liquid rocket engine components due to their low density, good formability, and excellent corrosion resistance [3,4]. However, a persistent strength-ductility trade-off has been observed in conventional Ti at cryogenic temperatures [5-8]. Coarse-grained (CG) Ti, when appropriately alloyed, exhibits good cryogenic ductility partially due to twinning-induced plasticity [9] but its strength is limited [10]. Conversely, ultrafine- or nano-grained Ti can be much stronger at cryogenic temperatures but typically has very low ductility as measured by uniform elongation during tension [11]. For instance, Sun et al. [6] reported the systematic decrease of ductility in ultrafine-grained (UFG) Ti compared to CG samples, tested at a wide range of deformation temperature down to 77 K. Consequently, the conventional microstructure design in Ti appears falling into a thorny dilemma between strength and ductility concerning cryogenic mechanical performance, similar to the strength-ductility trade off at room temperature [5-7,12].

To retain or improve ductility, it is critical to maintain a sustained strain hardening rate higher than the flow stress during tensile testing, according to the Considère criterion [13]. Cryogenic temperatures may influence ductility in two opposite ways. Firstly, low temperature suppresses the dynamic annihilation of dislocations, thus promoting strain hardening to improve ductility [14]. Secondly, low temperature could increase flow stress, due to the thermal nature of lattice friction stress for dislocation slip [15], which reduces ductility. For homogenous Ti, grain refinement does not appear to effectively retain ductility at cryogenic temperatures in order to overcome the strength-ductility trade-off [5-8, 12].

Another microstructure design paradigm, known as heterostructuring, has been recently proposed for improving the strength and ductility [16,17]. Numerous studies have invoked this strategy to mitigate or

* Corresponding authors.
E-mail addresses: xiaolong.ma@cityu.edu.hk (X. Ma), chxhuang@scu.edu.cn (C. Huang).

https://doi.org/10.1016/j.actamat.2024.119982
Received 8 January 2024; Received in revised form 8 April 2024; Accepted 6 May 2024
Available online 6 May 2024

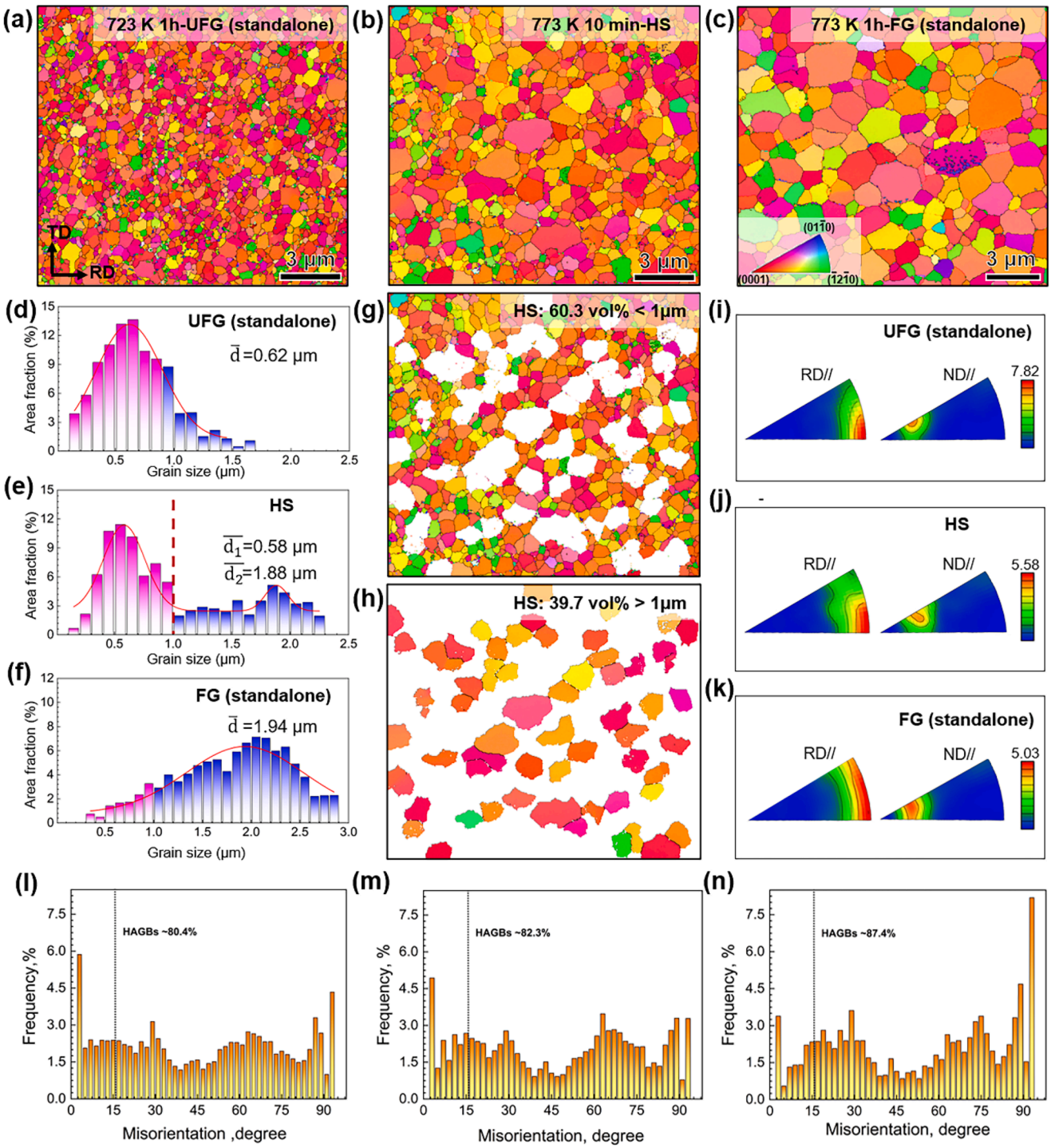

Fig. 1. EBSD characterizations of homogeneous and HS Ti samples. (a) Inverse pole figure (IPF) mappings of the sample annealed at 723 K for 60 min. (b) IPF mappings of the sample annealed at 773 K for 10 min. (c) IPF mappings of the sample annealed at 773 K for 60 min. (d-f) Grain size distribution in three samples. (g-h) Micrographs of the splitting of grains into two groups using 1 μm as the threshold i.e., >1μm (FG) and <1μm (UFG) for the sample annealed at 773 K for 10 min. (i-k) Inverse pole figures showing micro-texture similarities. Grain boundary misorientation angle distributions of (l) UFG-Ti, (m) HS-Ti, (n) FG-Ti collected from EBSD, highlighting the dominant portion of high-angle grain boundaries.

even evade the strength-ductility trade-off across a wide range of metals and alloys, primarily at room temperature [18-21] and occasionally in face-centered cubic (FCC) metals at low temperatures [22]. The underlying mechanism of this strategy is the interactive coupling between different zones during deformation. Mechanical incompatibility between heterostructured (HS) zones leads to inter-zone strain partitioning, resulting in local strain gradient and generation of geometrically necessary dislocations (GNDs) near interfaces [23,24]. This phenomenon, also referred to as hetero-deformation-induced (HDI) strengthening and hardening, promotes both strength and ductility [25,26]. A prominent example in published studies is, in fact, the HS Ti [24,27-31]. Notably, in spite of disparate zone constituents and architectures, heterostructures such as lamella structure and multimodal grain structure all exhibit substantially improved strength and ductility for Ti at room

temperature.

This naturally raises a question whether the heterostructure strategy has the potential to overcome the strength-ductility trade-off of Ti at cryogenic temperatures. Specifically, can the HDI strain hardening effectively counteract the increase in flow stress during cryogenic tensile deformation, thereby delaying necking? If so, what is the underlying effect of temperature on deformation of heterostructures?

To address these questions, we investigated the cryogenic (77 K) mechanical performance of a HS Ti, which consists of fine-grained (FG) zones embedded in UFG matrix zones. To enable a direct comparison, we also prepared standalone FG and UFG samples and tested their room-temperature mechanical behaviors. We demonstrate that the mechanical properties of HS Ti defy the strength-ductility trade-off established by standalone FG and UFG samples at 77 K – a phenomenon not observed at room temperature. We argued that the fundamental mechanisms underpinning this anomalous improvement of cryogenic mechanical performance in HS Ti are two-fold. One is the amplified inter-zone mechanical incompatibility at low temperature, leading to pronounced strain partitioning and generation of more GNDs; the other is the suppression of dislocation cross-slip at low temperature, which promotes dislocation pile-up, a more effective configuration for GNDs to produce HDI stress. Insights gained from this work will provide critical guidance for designing high-performance structural materials for cryogenic applications.

2. Experimental procedures

2.1. Materials fabrication

A commercially pure Ti (Grade 2) with a chemical composition of Ti-0.03 at.% N-0.08 at.% C-0.015 at.% H-0.3 at.% Fe-0.25 at.% O was used in this work. The commercial Ti bar with a diameter of 120 mm was vacuum annealed at 800 °C for 2 h to obtain a uniform CG structure with an average grain size of 44 μm (*Supplementary* Fig. S1). The annealed bar was hot and multi-pass extruded to rods with a diameter of 30 mm at 773 K. Then, 10 mm-thick plates were cut and rolled under liquid nitrogen temperature to the thickness of 1 mm in order to impart severe cold work and stored energy to promote recrystallization. Three groups of rolled samples were then annealed at 723 K for 60 min, 773 K for 10 min and 773 K for 60 min to obtain homogeneous and HS recrystallized microstructures.

2.2. Mechanical testing

The tensile specimens were dog-bone shaped with gauge dimensions of 12 mm in length, 2 mm in width and 1 mm in thickness. Each tensile test was repeated five times to ensure data repeatability, utilizing an Instron 5966 machine. The uniaxial stretching direction was parallel to the rolling direction and the strain rate was $5 \times 10^{-4}\ s^{-1}$. The cryogenic tensile tests were performed at 77 K and samples were bathed in liquid nitrogen for 3 min prior to testing. To elucidate temperature effect on mechanical properties and deformation mechanism, room-temperature tensile tests were also conducted in parallel on samples with the identical processing history, gauge geometry and testing parameters.

The loading-unloading-reloading procedure in the tensile test was performed at both room temperature and liquid nitrogen temperature, employing a strain rate of $5 \times 10^{-4}\ s^{-1}$. The specimens had a length of 15 mm and a width of 2.5 mm. An extensometer was employed for measuring the tensile strain. Following a series of specific unloading strains, the specimens were unloaded to 20 N using load control mode at a rate of 200 N/min, after which they were reloaded to the identical applied load.

2.3. Microstructure characterization

The microstructures of the samples before and after tensile tests were characterized by electron backscattering diffraction (EBSD, FEI Quanta 650F) and transmission electron microscopy (TEM, FEI Tecnai F20). The EBSD data were processed using HKL Channel 5 software. Samples used for EBSD measurements were electrolytically polished using a solution of 10 vol.% perchloric acid plus 90 vol.% methanol. The flakes used for TEM testing were mechanically polished to a thickness of 50 μm, followed by ion milling to perforation. The grain size (d) distributions in micrographs were evaluated using the linear intercept method (ASTM

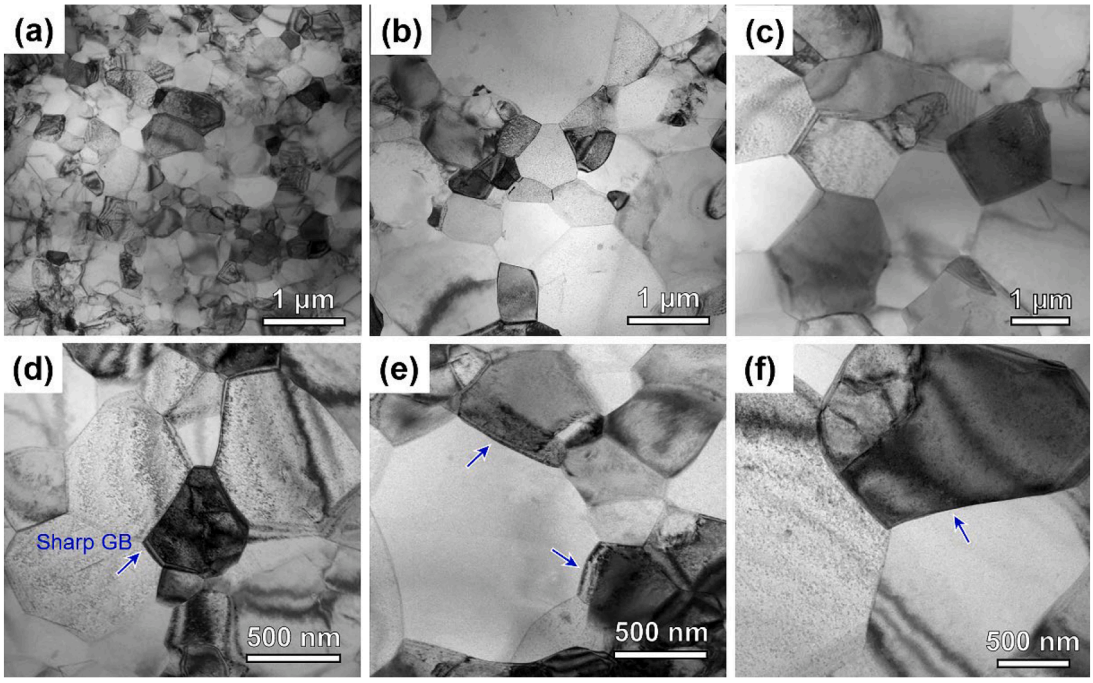

Fig. 2. TEM micrographs of homogeneous and HS Ti specimens. (a) UFG sample, (b) HS sample, (c) FG sample and the magnified micrographs in (d-f), revealing recrystallized microstructures.

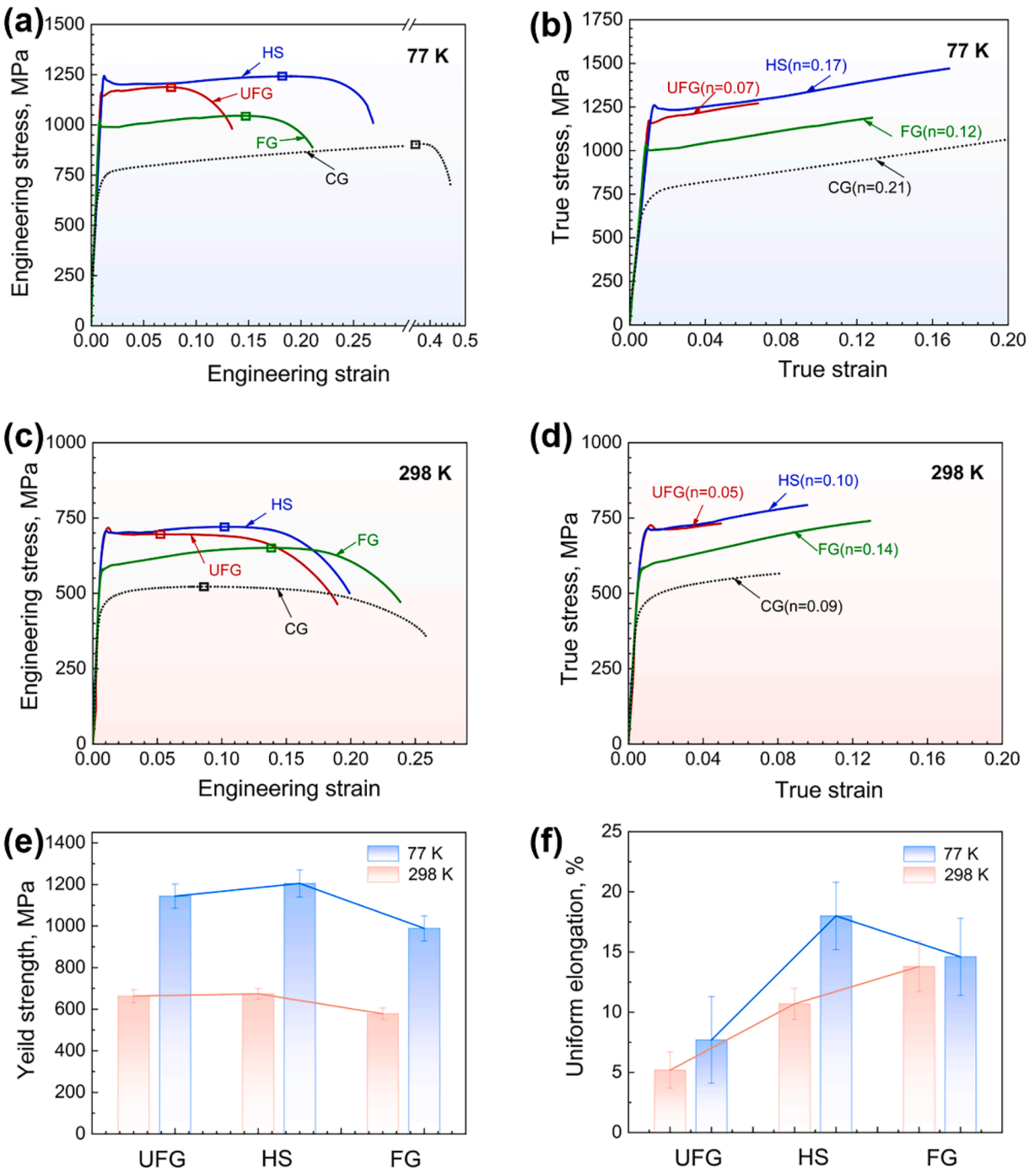

Fig. 3. Tensile mechanical behaviors of homogeneous and HS Ti. (a) Engineering and (b) True stress-strain curves at 77 K, (c) Engineering and (d) True stress-strain curves at 298 K. The small square frames on the curves in (a) and (c) marked the tensile strength. The work-hardening indexes (n) are presented near the curves in (b) and (d). (e-f) Histograms showing comparison of yield strength and uniform elongation at 77 K and 298 K.

E112–10).

In-grain misorientation axis (IGMA) within deformed grains were investigated based on the microstructure analysis using EBSD. The IGMA distribution for a specific deformed grain was determined utilizing the Channel 5 software. The following steps were performed: (1) Grains of interest were selected and orientation information for all interior pixels was extracted. (2) The misorientation above 1.2° was determined for all adjacent pixels. Misorientation lower than 1.2° was regarded from stochastic error in measurement. (3) The density of corresponding lattice rotation axes was calculated (measured in multiple uniform distributions, m.u.d.). More than 30 grains were randomly selected for each sample, and the IGMA intensity of four representative rotation axes, i.e., ⟨0001⟩, ⟨10–10⟩, ⟨10–12⟩, and ⟨13 −8–53⟩, were extracted from each grain. (4) The average was calculated to obtain an estimated IGMA intensity for the rotation axes of the sample.

Dislocation densities were qualitatively estimated using X-ray diffraction (XRD) and the modified Williamson-Hall method [32,33], which considering the anisotropy of the elasticity of different crystal planes. The modified formula is:$\Delta k = \frac{0.9}{D} + \sqrt{\frac{\pi A b^2}{2}\rho}\bar{g}\bar{C}$, where g is the reciprocal vector and Δk is the displacement of the diffraction reciprocal vector (obtained by the formula: $\Delta k = \frac{cos\theta \Delta 2\theta}{\lambda}$, $\Delta 2\theta$ is the measured

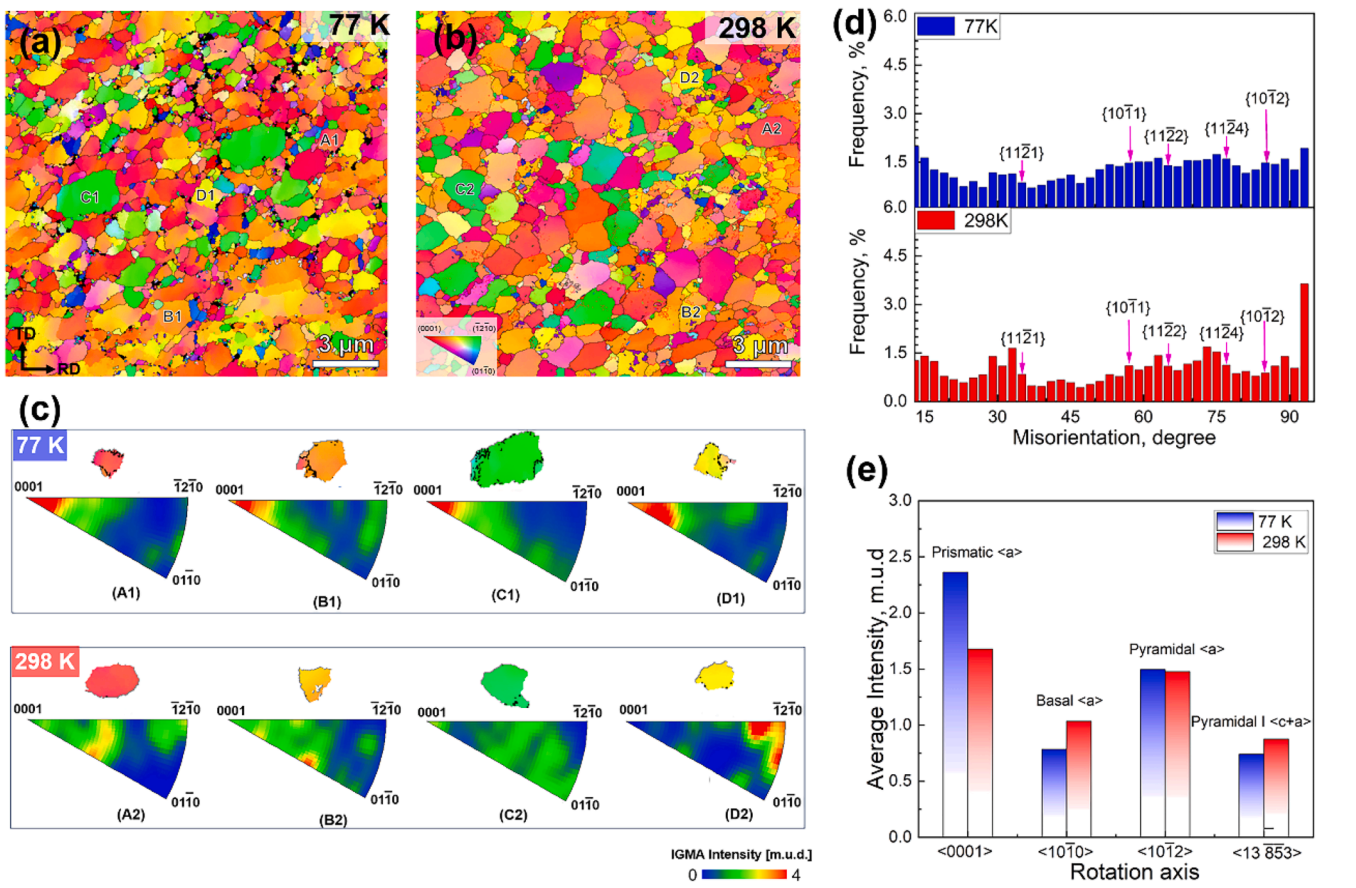

Fig. 4. Microstructural analysis of HS Ti specimens deformed to necking at 77 K and 298 K. (a) IPF map of the sample deformed to necking at 77 K. (b) IPF map of the sample deformed to necking at 298 K. (c) IGMA intensity distribution for representative grains numbered A1-D1 from (a) and A2-D2 from (b). (d) Grain boundary misorientation angle distribution of HS specimens deformed to necking at 77 K and 298 K. (e) Statistics for IGMA intensity distribution on lattice rotation axes that correspond to Prismatic ⟨*a*⟩, Basal ⟨*a*⟩, Pyramidal ⟨*a*⟩ and Pyramidal I ⟨*c* + *a*⟩ slips at 77 K and 298 K.

FWHM); D is grain size; A is a constant; b is the Burgers vector of materials; $\bar{c}$ is dislocation factor. The XRD experiments were performed on a Bruker D8 discovery test machine at 42 kV using Cu Kα radiation (λ = 0.15418 nm) with a scanning range of 30°−80° and a speed of 0.04° s^{-1}.

3. Results

3.1. Microstructures in homogeneous and HS Ti samples

Fig. 1 shows the typical inverse pole figure (IPF) mappings and grain size distributions of Ti samples annealed under different conditions. All three samples exhibit equiaxed grains, the microstructure characteristics of which are primarily governed by recrystallization (Figs. 1a-c). The 773 K-10 min sample demonstrates a bi-modal grain-size distribution, consisting of UFG zones (<1 μm) and FG zones (>1 μm). Figs. 1g-h reveal that FG zones occupy 40 % of volume, and UFG zones account for the rest 60 %. The segmentation also marks a prominent spatial configuration for grains – fine grains are discretely distributed, each being completely confined by ultrafine grains. This unique microstructure resembles the harmonic heterostructures in early reports [16,29]. The 723 K-60 min sample and the 773 K-60 min sample have grain size distributions comparable to the respective UFG and FG zones of the HS Ti (Figs. 1d-f). Hereafter, we refer to the 723 K-60 min and 773 K-60 min samples as UFG-standalone and FG-standalone samples, respectively. Crystallographic textures and grain structures are further characterized. In Figs. 1i-k, textures in all three samples demonstrate a strong retention of (0001) texture tilted approximately 30° from the normal direction (ND), as perceived by prior reports on recrystallized α-Ti [34,35]. Additional data on grain boundary misorientation angle distribution in Figs. 1l-n lend further credence to the recrystallization-dictated structures. Note in all three samples, high angle grain boundaries (HAGBs) take up more than 80 % of all grain boundaries.

To reveal the details of recrystallized microstructures in three samples, respective TEM micrographs for each condition are shown in Fig. 2. Both the low- and high-magnification micrographs demonstrate stark diffraction contrast from one grain to another, accompanied by some bending contours due to the foil thickness effect. The relatively pristine crystals with limited intragranular dislocation and sharp grain boundaries (marked by the blue arrows in Figs. 2d-f) in all three samples are in line with the recrystallized microstructure identified by EBSD results.

Summarizing the microstructure characteristics of the three samples of interest, one can safely conclude that the dominating difference among them is the size distribution and spatial configuration of grains while other features such as texture component and dislocation density resemble each other *(Supplementary Fig. S2)*. Hence, the HS sample is composed of two groups of grains, each having a comparable size with the respective standalone FG and UFG samples. Such similarity and discrepancy in recrystallization structure allow us to dedicatedly resolve the effect of harmonic grain structure heterogeneity on mechanical properties by excluding other microstructural factors.

3.2. Tensile properties at cryogenic and room temperatures

Figs. 3a-d show the uniaxial tensile curves of three recrystallized samples along with the conventional CG behavior as reference, tested at

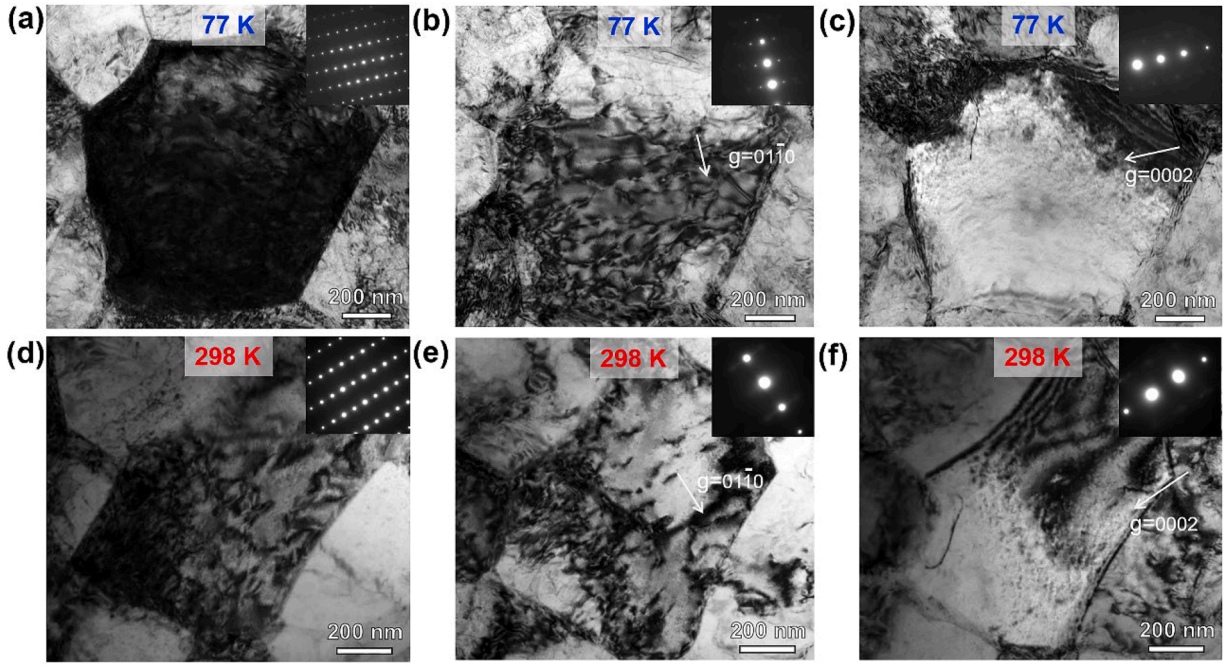

Fig. 5. [11-20] on-zone and two-beam condition TEM micrographs of a HS specimen deformed to ~10 % strain. (a-c) deformed at 77 K, (d-f) deformed at 298 K.

cryogenic and room temperatures (77 K and 298 K). The mechanical properties are also visualized by histograms in Figs. 3e-f to facilitate a direct comparison. At 77 K, the HS sample exhibits the most appealing properties, with its yield strength, ultimate strength and uniform elongation all outperforming those of UFG and FG samples (Fig. 3a). In addition, the work-hardening index (n) obtained using the Holloman formula ($\sigma_T = K\varepsilon_T^n$) also suggests that the HS sample has a hardening capacity ($n = 0.17$) beyond FG ($n = 0.12$) and UFG ($n = 0.07$) counterparts (Fig. 3b). Thus, despite being a mixture of FG and UFG constituents, the HS sample defies the property trade-off established by its two constituents at the cryogenic temperature. This demonstrates the capability of the heterostructure to achieve strength and ductility superior over its zone constituents at the cryogenic temperature, a trait that has not been appreciated before. Statistics of repeated tests reaffirm this anomalous but intriguing phenomenon (*Supplementary Fig. S3*).

These counterintuitive performances at the cryogenic temperature motivate a parallel comparison to room-temperature behaviors. Strikingly, room-temperature tensile properties of the HS sample (Figs. 3c-d), particularly uniform elongation and working hardening index fall between those of the other two samples, i.e., still under the spell of property trade-off. Additionally, we note that cryogenic ductility of the HS sample exhibits 70 % improvement compared to its room-temperature performance, far exceeding those of UFG- and FG-standalone samples. In fact, the FG-standalone sample becomes even less ductile at the cryogenic temperature. The comparison suggests that heterostructure is capable of gaining extra strain hardening and ductility beyond its domain components at cryo-temperatures, which is much appealing but has yet to be fully analyzed in early studies.

3.3. Deformed microstructures after tension

The deformed microstructure analyses primarily focus on the HS Ti sample for the following two reasons. Firstly, since its microstructure can be approximately regarded as the blend of UFG and FG samples, the UFG and FG zone interiors in HS samples are expected to inherit the primary features of deformed microstructure in their standalone counterparts. Secondly, the HS sample evades the property trade-off at the cryogenic temperature. Therefore, the evolution of its deformed microstructure is naturally of most interest to elucidate the mechanistic origin of its superior properties.

To uncover the origin of anomalous improvement of cryogenic mechanical performance in HS Ti, we first characterize the deformed microstructure and identify the deformation mode. Similar to room-temperature conditions, dislocation slip remains the primary plasticity carrier, while deformation twinning is limited. In Figs. 4a-b, IPF maps of the uniformly deformed region upon fracture reveal rare presence of twinning in both UFG and FG zones, regardless of deformation temperature. The scarcity of deformation twins in both UFG and FG zones are further supported by the grain boundary misorientation angle distributions (Fig. 4d), which does not signify prominence of any type of twins after deformation compared to their initial states (Fig. 1m).

Regarding dislocation slip, IGMA is conducted to assess the propensity of each slip mode with significant statistics. Each slip system corresponds to a respective crystallographic axis for lattice rotation, and the intensity of in-grain rotation axes represents the relative propensity of different slip modes [36,37] (see details in *Supplementary Fig.S4 and Supplementary note 1*). Fig. 4c showcases the IGMA of random grains, depicting the intragranular rotation axis distribution in the microstructure deformed to necking at both temperatures. Each rotation axis, representing a slip system, exhibits an intensity in the orientation space representation. We average this intensity for major slip systems in HS Ti over more than 30 grains in samples deformed at 77 K and 298 K, respectively, and present the statistics in Fig. 4e. Clearly, prismatic $<a>$ slip remains the dominant in cryo-deformation, while basal and pyramidal slips are relatively less operative.

Activation of dislocation slip is further confirmed by using dislocation imaging and the invisibility criterion of $\boldsymbol{g}\cdot\boldsymbol{b} = 0$ in Figs. 5a-f. It is found that pure $\langle a\rangle$ slip predominates while $\langle c\rangle$ component remains minimal in the observed grains regardless of the deformation temperature. We note some recent studies have reported the enhanced local activity of pyramidal $\langle c+a\rangle$ slip in HS Ti deformed at room temperature, which is ascribed to interface constraints [28,38]. The cryogenic temperature, though, does not seem to heighten the role of pyramidal slip according to the global statistics revealed here.

The dislocation densities in uniformly-deformed regions of FG-standalone, UFG-standalone and HS samples deformed to 5 % are analyzed by XRD. The width and intensity of Bragg peaks in XRD are significantly influenced by grain size and lattice strain. Therefore, one

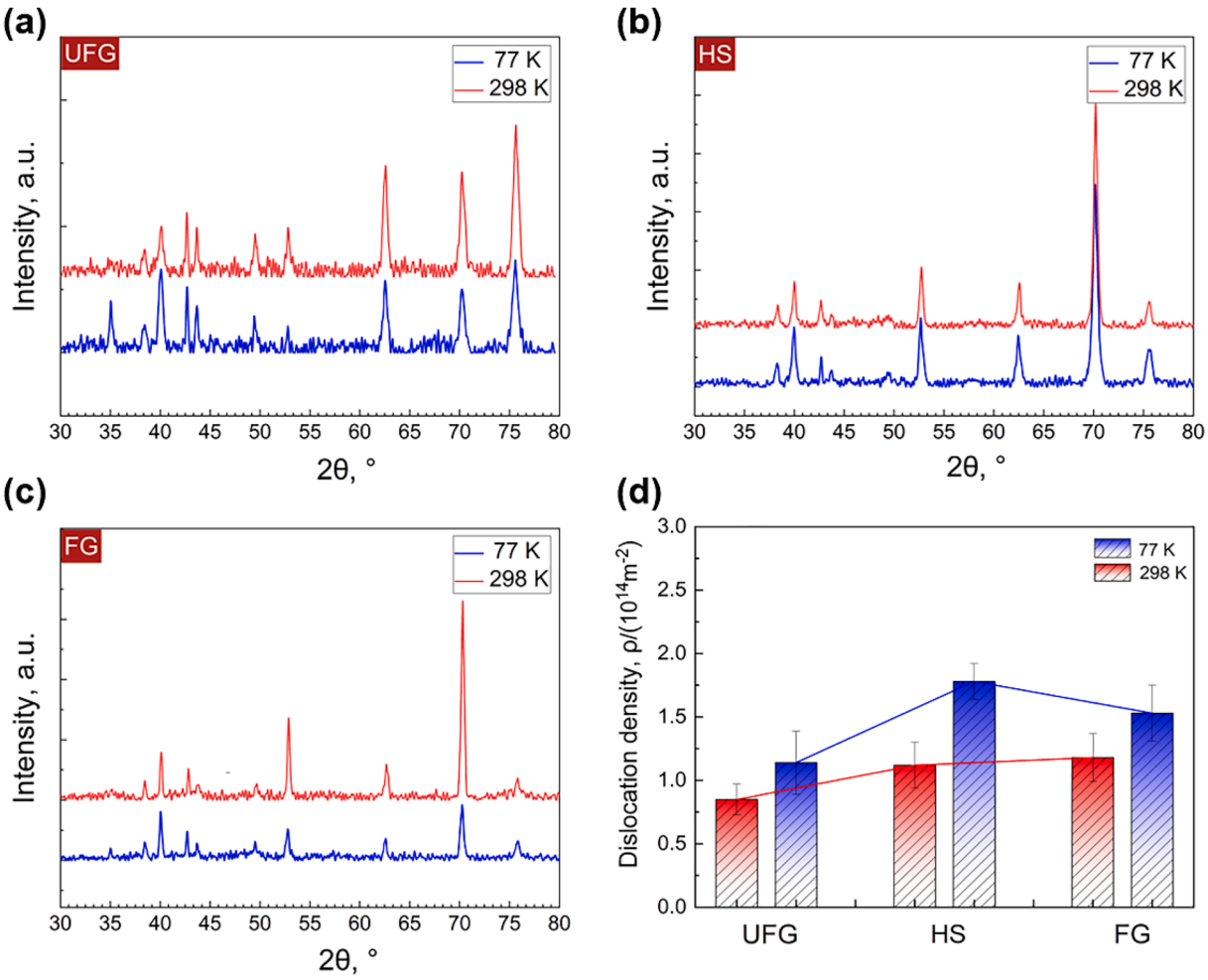

Fig. 6. XRD diffraction patterns of three annealed specimens after tensile deformed to 5 % strain at 77 K and 298 K. (a) UFG-standalone sample, (b) HS sample, (c) FG-standalone sample, (d) Comparison of dislocation densities.

Table 1
Dislocation density measurement in HS Ti deformed to 5 % at 77 K and 298 K and rule-of-mixture estimate based on the homogeneous samples of identical deformation conditions.

	Measured dislocation density (ρ_m / 10^{14} m^{-2})	Rule-of-mixture calculated density (ρ_c / 10^{14} m^{-2})	Ratio of ρ_m to ρ_c (ρ_m/ ρ_c)
HS sample deformed at 77 K	1.78	1.30	1.33
HS sample deformed at 298 K	1.12	0.98	1.14

can qualitatively estimate dislocation densities under different deformation conditions using the modified Williamson-Hall method. The experimental results are shown in Fig. 6 and Table 1. Clearly, the results reveal that cryo-deformation always injects more dislocations into Ti samples compared to room-temperature cases despite the three different microstructures. This general trend can be rationalized by the mitigated dynamic annihilation/recovery at cryo-temperature, leading to a higher storage of dislocations. We further compare the measured dislocation density in HS sample to the rule-of-mixture estimate from two standalone homogeneous samples as per their volume fractions. Apparently, the HS sample exhibits a higher excess of dislocation density (the ratio of measured to calculated values in Table 1) at 77 K, more so than at 298 K. This indicates that the HS sample can generate and store significantly more dislocations at the cryogenic temperature.

3.4. HDI stress measured by load-unload-reload (LUR) tests

Fig. 7a-b show the LUR curves for HS Ti tested at 77 K and 298 K. The test parameters were identical to those of uniaxial tension. The HDI stress is obtained by the equation [39]:

$$\sigma_{HDI} = \frac{\sigma_r + \sigma_u}{2} \quad (1)$$

where σ_{HDI} represents the total HDI stress that conceptually contains both intra-zone and inter-zone components; σ_r is the reloading stress and σ_u is the unloading stress. The HDI hardening can be further assessed by

$$\Theta_{HDI} = \frac{d\sigma_{HDI}}{d\varepsilon_T} \quad (2)$$

where Θ_{HDI} is the slope of the line segment in Fig. 7c. For the strain range for stress evaluation, the HS exhibits stronger HDI hardening in cryo-deformation than room-temperature-deformation. In addition, the ratio of HDI stress σ_{HDI} (Fig. 7c) to the overall stress σ_0 (Fig. 7a) could serve as a measure for the role of HDI effect in the mechanical performance. As shown in Fig. 7d, compared to the room-temperature-deformation, this ratio is universally higher in cryo-deformation at all levels of strains. Taking these as a whole, the results indicate that HDI effect appears to play a more salient role at cryo-deformation compared

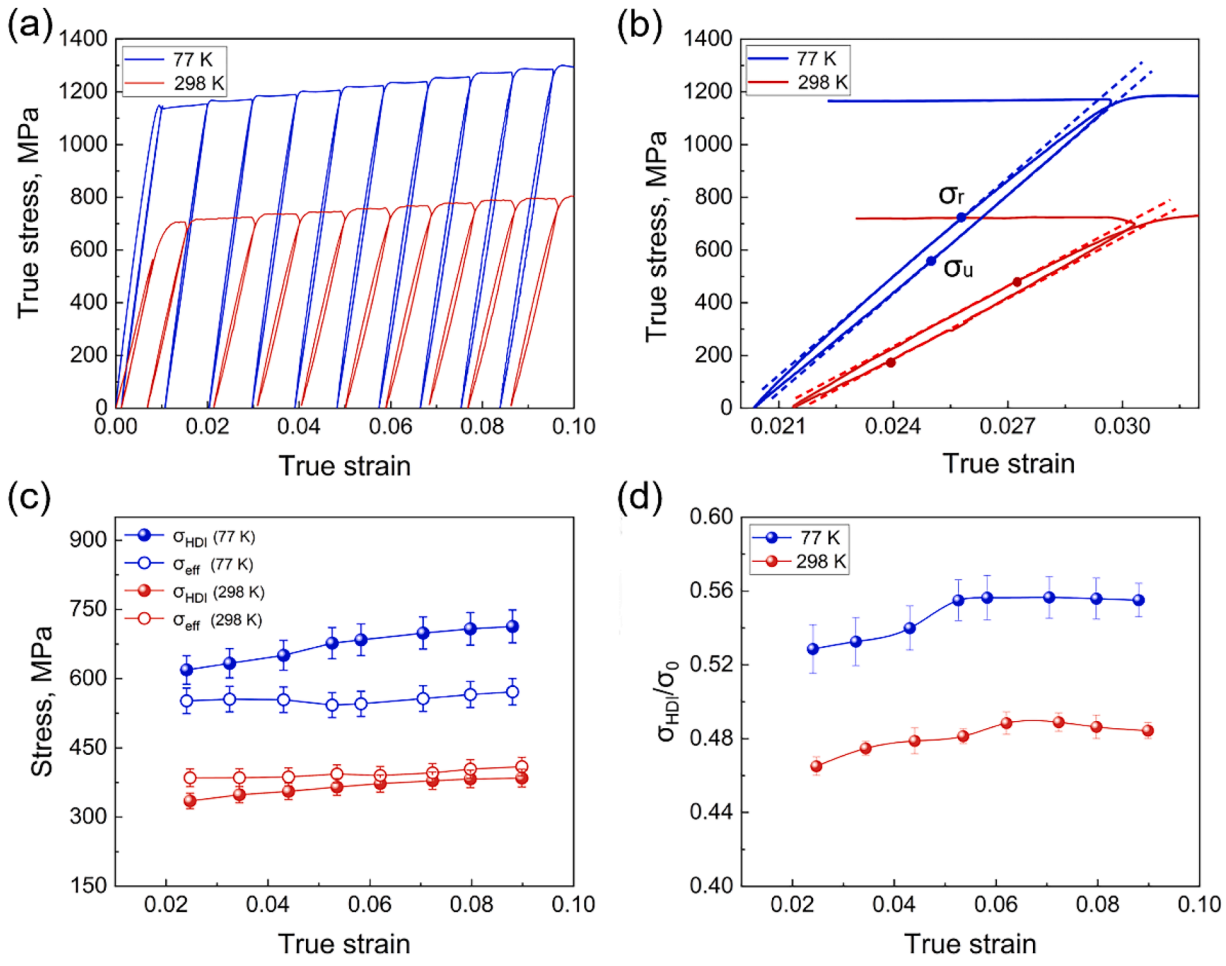

Fig. 7. Comparison of HDI stress of HS Ti at 77 K and 298 K. (a) LUR curves. (b) Magnified hysteresis loop. (c) Evolution of HDI stress σ_{HDI} and effective stress σ_{eff} calculated from the LUR curves in (a). (d) The ratio of HDI stress σ_{HDI} to the overall stress σ_0.

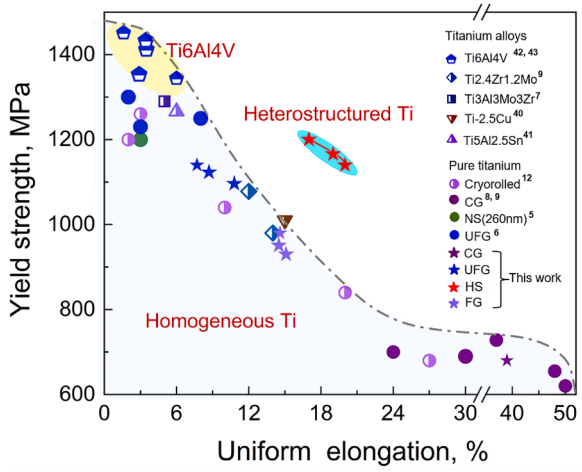

Fig. 8. Ashby plot of cryogenic strength and tensile uniform elongation for pure Ti and titanium alloy [5-9,12,41-44].

to room-temperature deformation.

4. Discussion

4.1. Superior cryogenic strength-ductility synergy of HS Ti

We highlight the cryogenic mechanical performance of the HS Ti against previously published data on the strength-elongation Ashby plot (Fig. 8). The strength-ductility synergy of our HS Ti surpasses that of pure Ti and even certain dilute alloys with homogeneous grain structures at cryogenic temperatures. The exceptional mechanical properties, coupled with the alloy-free microstructure, position HS pure Ti as a promising alternative to alloys in cryogenic applications, particularly in cryogenic vessels, pipelines, and liquid rocket engines, where composition-sensitivity or material cost is a concern. For data consistency, literature data surveyed in Fig. 8 only encompass results from bulk testing (no less than 1 mm for any gauge region) as miniature samples are more susceptible to size effects and measurement errors [40].

4.2. Deformation modes in HS Ti at cryo-temperature

To understand the underlying mechanisms for the anomalous improvement of cryogenic mechanical properties in HS Ti, we firstly attempt to analyze its deformation modes, focusing on two aspects – first, addressing the scarcity of mechanical twinning in deformed microstructure even at the cryogenic temperature; second, identifying the major slip system in the tensile deformation.

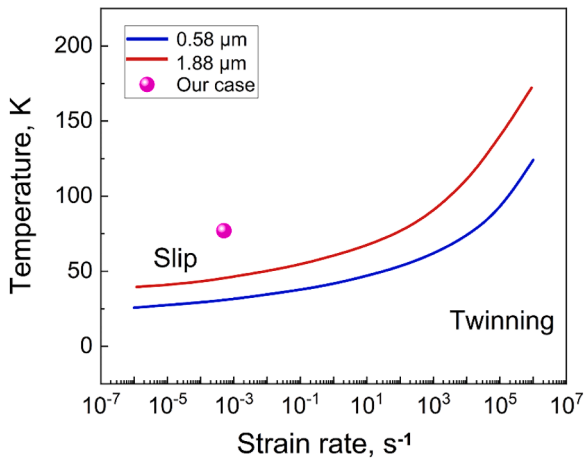

Fig. 9. Calculated slip-twinning transition lines for two grain size modals (0.58 μm and 1.88 μm) in HS Ti. Upper left to transition line is for slip and lower right to it is for twinning. The transition condition for temperature and strain rate is determined when the slip stress τ_{slip} becomes equal to the twinning stress τ_{twin} (*Supplementary Note 2*).

Table 2
The average Schmid factor for prismatic ⟨*a*⟩, basal ⟨*a*⟩, pyramidal ⟨*a*⟩ and pyramidal I ⟨*c* + *a*⟩ in HS Ti at 77 K.

	Various Slip Systems			
	{10–10}<1 − 210> prismatic <*a*>	{0002}< 11−20> basal <*a*>	{10–11}<1 − 210> pyramidal <*a*>	{10–11}<− 1–123> pyramidal *I* < *c* + *a*>
Average Schmid factor	0.45	0.14	0.39	0.47

Considering first the mechanical twinning, it is often perceived as the primary cause for the enhanced ductility of CG Ti at cryogenic temperatures [9], which is consistent with the CG data presented in our Fig. 3a. This is because low temperature usually promotes twinning by either altering the twinning stress or elevating the flow stress by inhabiting dynamic recovery [45,46]. However, twinning is also strongly dependent on grain size. Alteration in grain size mediates the competition between dislocation slip and twinning as the dominant deformation mode. For grain size more than 100 nm, reducing grain size usually leads to a faster increase in critical stress required for twinning than for dislocation slip [46]. Thus, below a critical size for which critical stresses for both modes are equivalent ($\sigma_{slip} = \sigma_{twin}$), dislocation slip governs the deformation and mechanical twinning diminishes. This critical grain size becomes smaller as temperature drops or strain rate increases. To specially elucidate our case, we invoke the analysis from Meyers et al. [46] and apply to our pure Ti (*Supplementary note 2)*. Fig. 9 demonstrates the slip-twinning transition for two grain size modals in HS Ti. Apparently, at 77 K and a strain rate of $5 \times 10^{-4}\, s^{-1}$, mechanical twinning is not favored and dislocation slip dictates the tensile deformation of all presented Ti samples.

Regarding the dominant slip system, texture also needs to be taken in accounts. The recrystallized microstructure manifests a strong basal pole roughly aligned with the ND. Thus, when pulled along the transverse direction (TD)- rolling direction (RD) plane, at least one set of the prismatic planes are expected to have a significantly higher Schmid factor (SF) than all the basal. The average SF for prismatic ⟨*a*⟩, basal ⟨*a*⟩, pyramidal ⟨*a*⟩ and pyramidal I ⟨*c* + *a*⟩ are listed in Table 2. Provided that the prismatic slip has the lowest critical resolved shear stress (CRSS) at cryogenic temperatures [47,48] and the highest SF according to Schmid's law analysis (*Supplementary note 3*), one prismatic slip system could be envisioned to indeed govern the cryo-deformation.

4.3. Pronounced strain partitioning in HS Ti during cryo-deformation

The primary deformation mode itself cannot explain the anomalous

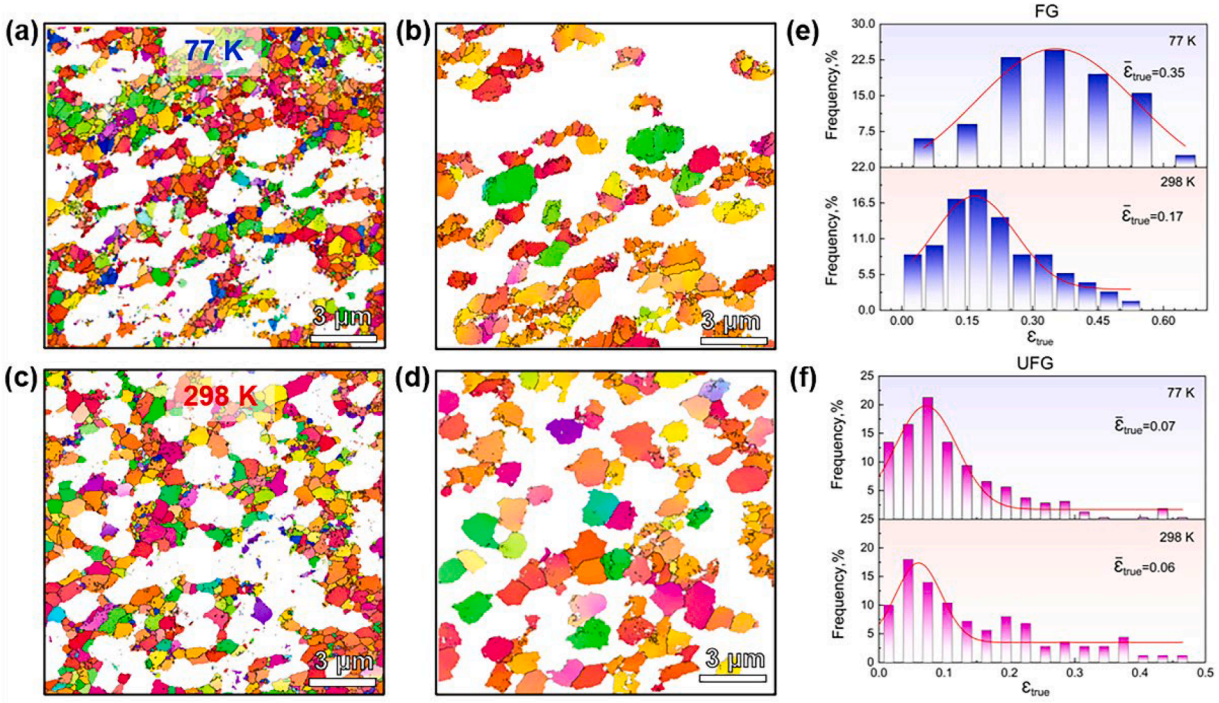

Fig. 10. Strain partitioning between FG zones and UFG zones at 77 K and 298 K. Grain morphology of (a) UFG zones (<1 μm) and (b) FG zones (>1 μm) in the HS Ti sample deformed to necking at 77 K. Grain morphology of (c) UFG zones (<1 μm) and (d) FG zones (>1 μm) in the HS Ti sample deformed to necking at 298 K. Distribution of true strain carried by (e) FG zones and (f) UFG zones at 77 K and 298 K.

Table 3
Strain partitioning analysis for HS Ti in respective deformation at 77 K and 298 K.

	Volume fraction	Average grain-level strain upon necking		Normalized strain contribution to overall plastic deformation	
		77 K	298 K	77 K	298 K
FG zones	39.7 %	0.35	0.17	76.7 %	65.1 %
UFG zones	60.3 %	0.07	0.06	23.3 %	34.9 %

improvement of cryogenic mechanical property in the HS Ti since it is shared by both homogeneous and HS Ti samples. To delve deeper, we investigated the strain partitioning in the HS samples by tracking changes in grain morphologies and sorting them according to their UFG or FG origin. The true strain carried by an individual grain is calculated based on its aspect ratio α using the formula $\varepsilon = (2/3)\ln\alpha$ and assuming $\alpha = 1$ for equiaxed grains at beginning [24]. Figs. 10a-f present the statistics from over 300 grains in the HS Ti deformed to necking at both temperatures. Notably, FG zones after cryo-deformation carry more plastic strain compared to those after room-temperature deformation. We further normalized the strain partitioning by considering the volume fractions of each type of zones (Table 3) to enable a consistent comparison, revealing that FG zones carry ~76 % of the strain in cryo-deformation and ~65 % at room temperature, with the rest being accommodated by UFG zones. Evidently, the strain partitioning in the HS sample is statistically higher in cryo-deformation than at room temperature, which is a crucial finding.

This heightened strain partitioning in post-yield deformation has profound implications for the work hardening capacity in HS Ti at the cryogenic temperature (as indicated by work hardening index in Fig. 3b). At the microscale, the increased strain gradient near the zone interfaces leads to a higher GND density according to strain gradient plasticity [49,50] since dislocation slip is the dominant deformation mode as established earlier. Consequently, this pronounced strain partitioning contributes to the increase in two primary dislocation-density-based terms in the hardening expression for heterostructure –Taylor stress ($\Delta\sigma_{Taylor}$) and HDI stress ($\Delta\sigma_{HDI}$) [51-53]. Firstly, the increase of GND density makes a direct contribution to the $\Delta\sigma_{Taylor}$ by elevating the total dislocation density, as substantiated by XRD measurements in Fig. 6. Notably, at 77 K, the actual dislocation density in the HS Ti significantly exceeds the estimate based on the rule of mixture using homogeneous samples, more so than at 298 K (Table 1). Secondly, the elevated GND density during cryo-deformation also leads to an enhanced $\Delta\sigma_{HDI}$. The ratio of HDI stress to the overall stress is consistently higher in cryo-deformation at various strain levels (Fig. 7d), substantiating the heightened role of the long-range stress during the deformation at the cryogenic temperature. Altogether, it is indicated that the pronounced strain partitioning and the intensified hetero-deformation effect contribute to the cryogenic effect, driving the anomalous improvement of cryogenic mechanical performance in HS Ti.

4.4. Origins of cryogenic impact on HS Ti

4.4.1. Temperature-dependent mechanical incompatibility

The observed cryogenic impact on mechanical performance of HS Ti involves complementary mechanisms that operate at different length scales. At the microstructure zone level, the cryogenic temperature

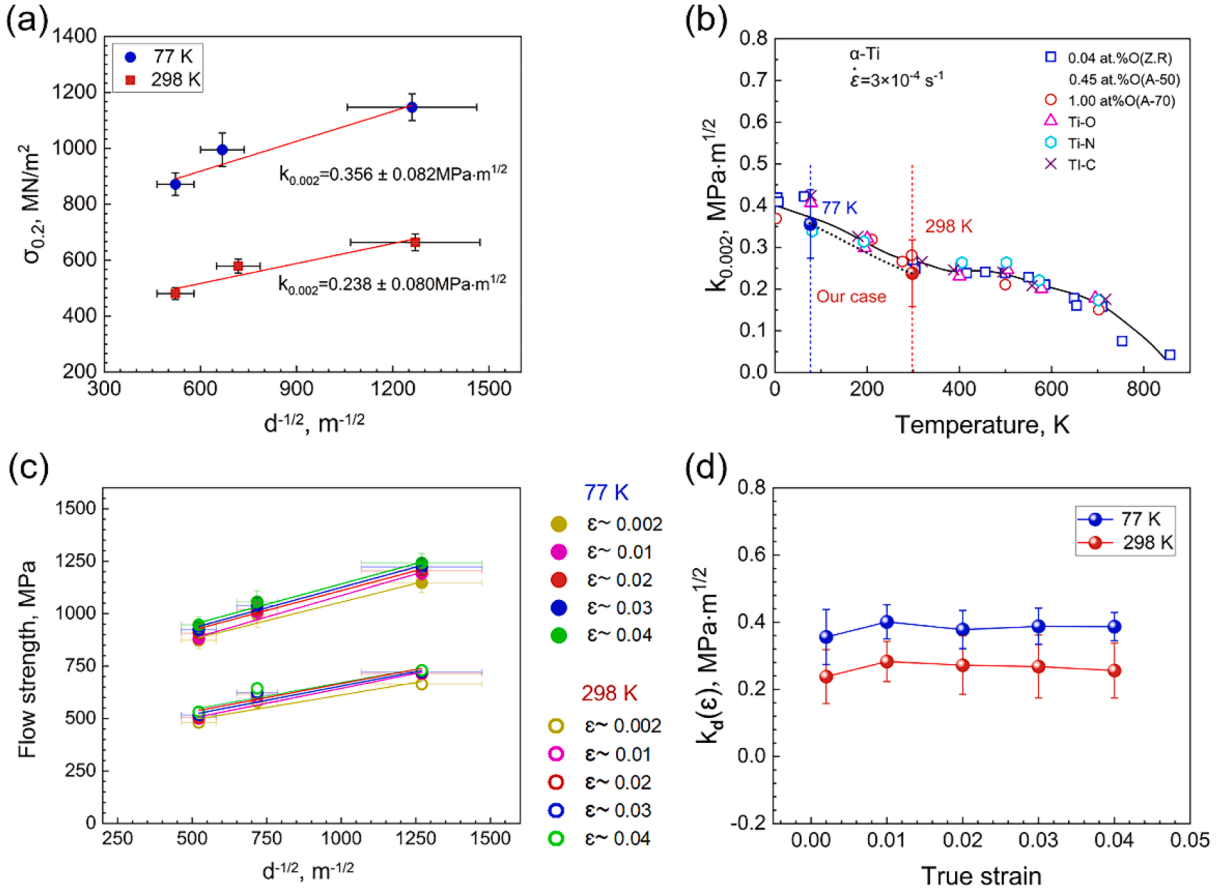

Fig. 11. Temperature-dependent Hall-Petch constant k_d in pure Ti. (a) Experimental measurement of Hall-Petch constant at 77 K and 298 K. (b) Conrad's summary of temperature-dependent k_d in Ti with different interstitial elements and contents [57-62]. (c) Experimental measurements of Hall-Petch coefficients $k_d(\varepsilon)$ with different applied strain at 77 K and 298 K. (d) Curves of $k_d(\varepsilon)$ versus applied strain at 77 K and 298 K.

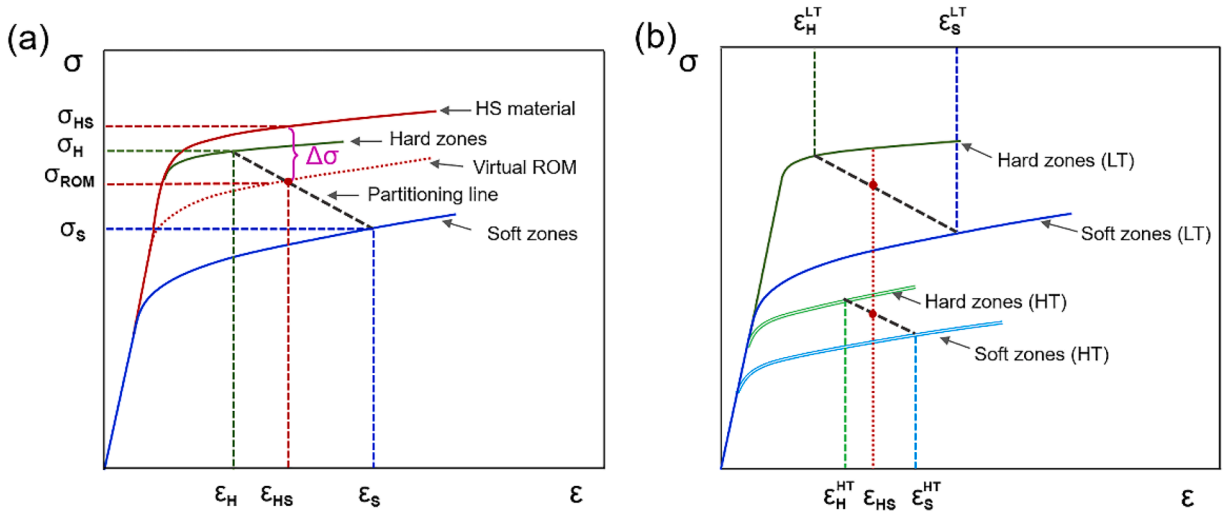

Fig. 12. (a) Schematic illustration of mechanical incompatibility inducing strain partitioning ($\Delta\varepsilon = \varepsilon_S - \varepsilon_H$) in heterostructure during plastic deformation. (b) Diffrerent extents of strain partitioning due to altered mechanical incompatibility at two deformation temperatures.

magnifies the flow behavior difference between FG and UFG zones, thereby amplifying the mechanical incompatibility during deformation. The difference in yield strength caused by grain sizes is determined by the coefficient (k_d) in the classical Hall-Petch relationship below:

$$\sigma = \sigma_0 + k_d(T, \dot{\varepsilon})d^{-1/2} \tag{3}$$

where σ_0 is a constant and usually represents the lattice friction stress for dislocation slip in the material; k_d is the Hall-Petch coefficient and is a function of deformation temperature and strain rate; d is average grain size. The phenomenological Hall-Petch relationship can be rationalized via multiple models [10], and dislocation pile-up model is probably one of the most used for reasoning, as deduced below [54,55]:

$$\sigma = \sigma_0 + \beta G b^{1/2} d^{-1/2} \tag{4}$$

where G represents the shear modulus; b is the magnitude of the Burgers vector; and β is a constant associated with crystal structure for polycrystalline materials. The pre-factor together $\beta G b^{1/2}$ corresponds to the Hall-Petch coefficient k_d. Clearly, k_d is positively correlated with the shear modulus (G). As temperature decreases, thermal vibration of atoms decreases, so does the equilibrium inter-atomic separation, i.e., thermal contraction upon cooling. In general, elastic moduli of metallic materials increase as their atomic separation decreases [56]. As the shear modulus increases with decreasing temperature (42.4 GPa at 298 K and 48.1 GPa at 77 K for Ti [57]), k_d becomes larger at lower temperatures. For the present samples, k_d was measured as 0.238 at 298 K and 0.356 at 77 K (Fig. 11a) by adding a sample with additionally different grain size *(Supplementary Fig. S5)*, consistent with Conrad's summary of temperature-dependent k_d values, as depicted in Fig. 11b [57-62].

For post-yield flow behaviors, we further analyzed the Hall-Petch coefficient $k_d(\varepsilon)$ as a function of strain (shown in Figs. 11c-d) – it almost remains invariant for different strain levels. Importantly, the value of $k_d(\varepsilon)$ is always higher at the low temperature, suggesting that the flow stress is consistently amplified at all strain levels when deformation temperature decreases.

4.4.2. *Mechanical incompatibility and strain partitioning*

The linkage between amplified mechanical incompatibility and inter-zone strain partitioning can be pictorially explained in Fig. 12. Fig. 12a illustrates the general case for strain partitioning and its impact on HS materials. The black dashed line intersecting stress-strain curves represents how strain partitions across hard and soft zones, which is hereafter referred to as *partitioning line*. Its slope, determined by the spatial configuration of the hard/soft zones and the loading direction with respect to this configuration, governs the partitioning law in the plastic deformation. Using laminates with alternative hard and soft layers as an example, strain partitioning is minimal when the tensile loading is parallel to layer interfaces (isostrain condition and the partitioning line is nearly vertical) and pronounced when the tensile loading is vertical to layer interfaces (isostress condition and the partitioning line is nearly horizontal). In more general configuration and loading conditions, the partitioning line is sketched in Fig. 12a and its exact solution of slope (m) relies on numerical simulation or experimental measurement. Using the measured respective strains (ε_H and ε_S) in constituent zones and lever-rule operation of their standalone stress-strain curves, one can predict the rule-of-mixture stress (σ_{ROM}) for each global strain level (ε_{HS}). This rule-of-mixture stress is virtual because actual response of stress needs to take the effect of heterogeneous deformation into accounts, which gives rise to the additional stress term ($\Delta\sigma$) containing two parts ($\Delta\sigma_{Taylor}$ and $\Delta\sigma_{HDI}$ in Section 4.3). According to the strain-gradient-plasticity-based HDI effect [21,49-50], the additional stress is positively correlated to the extent of strain partitioning ($\Delta\varepsilon = \varepsilon_S - \varepsilon_H$), i.e., $\Delta\sigma \sim \Delta\varepsilon$, because both of its two parts are so as elaborated in Section 4.3.

The extent of strain partitioning depends on both the partitioning line and disparity of flow behavior between standalone zone constitutes. The former is presumably insignificantly affected by the deformation temperature since the spatial configuration of the hard/soft zones and the loading direction are identical for room-temperature and cryogenic tension. The latter can be strongly influenced by temperatures and manifested in the temperature-dependent Hall-Petch coefficient, $k_d(T)$. In other words, strain partitioning in the same HS material can be expressed as a function of deformation temperature given the same global strain and the slope of partitioning line, $\Delta\varepsilon = f(T)|_{\varepsilon_{HS},\, m}$. Analytical determination of strain partitioning, $\Delta\varepsilon$, is nontrivial, as it involves solving a system of two-variable nonlinear equations. Here, we attempt to understand the general trend of strain partitioning using the geometry in Fig. 12b. Lower temperature gives rise to the amplified gap of flow behaviors in standalone hard/soft constituents. While the partitioning lines are assumed to share the common slope, the extent of strain partitioning is greater at the low temperature than the other ($\Delta\varepsilon^{LT} > \Delta\varepsilon^{HT}$). Consequently, the more pronounced strain partitioning will lead to a greater excess accumulation of GNDs near zone interfaces to boost hardening.

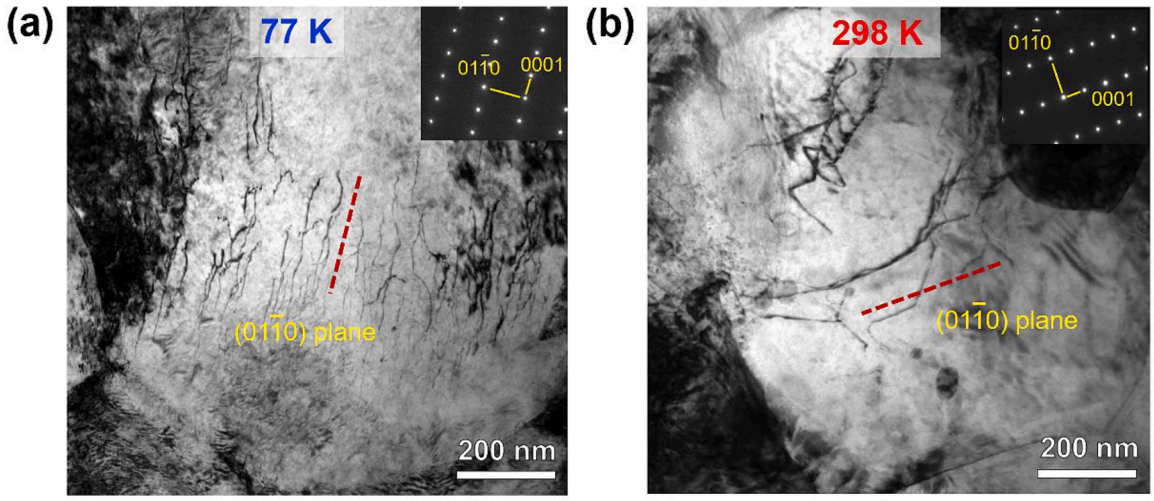

Fig. 13. TEM observation of dislocation slip behavior of HS samples deformed to ~3.8 % strain at (a) 77 K and (b) 298 K.

4.4.3. Temperature-dependent cross-slip tendency and GND configuration

At the dislocation motion level, low temperatures suppress cross-slip while favoring planar slip and dislocation pile-up, promoting HDI stress and hardening through effective GNDs pile-ups. The primary plastic carrier, prismatic $\langle a \rangle$, is reported to cross-slip recurrently to pyramidal planes that representing its ground state [63,64]. However, decreasing temperature progressively leads to an even higher Peierls friction stress in pyramidal planes compared to prismatic planes, making cross-slip significantly retarded at cryogenic temperatures [64,65]. Additional TEM observations of slip morphology at two temperatures lend credence to this view (Fig. 13). The prismatic slip exhibits a more planar fashion at 77 K with the dislocation lines primarily parallel to (01$\bar{1}$0) planes when viewed near [2$\bar{1}\bar{1}$0] axis. In contrast, dislocation lines become less constrained on prismatic planes, i.e., tendency for cross slip increases at 298 K. The cross-slip hindrance in the HS Ti promotes GNDs pile-up and enhances HDI hardening efficacy. As planar slip prevails, dislocations are more likely to pile up against zone boundaries. Compared to the stochastic arrangement patterns for dislocations, pile-up creates a more effective configuration of GNDs, resulting in long-range internal stress against subsequent slip [25]. This means the overall hardening is improved by boosting the $\Delta\sigma_{HDI}$ while maintaining an identical $\Delta\sigma_{Taylor}$.

5. Conclusion

In summary, this study reveals anomalous improvement of cryogenic mechanical properties in Ti with harmonic heterostructure, showcasing its ability to surpass the trade-off limitation observed in homogeneous Ti, a trait not observed at room temperature. The prismatic $\langle a \rangle$ slip remains the primary plastic carrier at 77 K, similar to deformation at 298 K. However, the cryogenic temperature induces pronounced strain partitioning and intensifies the hetero-deformation effect. These cryogenic impacts originate from two key aspects. Firstly, the temperature-dependent Hall-Petch effect leads to the greater inter-zone mechanical incompatibility at cryogenic temperature. Secondly, cross-slip is retarded at cryogenic temperature, favoring planar slip and dislocation pile-up, promoting high HDI stress through effective GNDs pile-up. Together, these factors contribute to the enhanced effectiveness of heterostructures at cryogenic temperature. The insights into cryo-deformation characteristics gained from this study is presumably extendable to other heterostructures and therefore pave the way for designing high-performance structural materials for cryogenic technologies.

CRediT authorship contribution statement

Wuli Su: Data curation, Investigation, Writing – original draft. **Mingsai Wang:** Data curation, Investigation. **Fengjiao Guo:** Data curation, Investigation. **Hao Ran:** Data curation, Investigation. **Qian Cheng:** Data curation, Validation. **Qingyuan Wang:** Investigation, Validation. **Yuntian Zhu:** Conceptualization, Supervision, Writing – review & editing. **Xiaolong Ma:** Conceptualization, Data curation, Investigation, Writing – original draft, Writing – review & editing. **Chongxiang Huang:** Conceptualization, Data curation, Investigation, Supervision, Writing – original draft, Writing – review & editing.

Declaration of competing interest

The authors declare that they have no known competing financial interests or personal relationships that could have appeared to influence the work reported in this paper

Acknowledgements

None.

Funding

This work was supported by the National Key R&D Program of China (No. 2021YFA1200202) and National Natural Science Foundation of China (No. 51931003 and No. 12302246).

Data and materials availability

All data are available in the main text or the supplementary materials.

Supplementary materials

Supplementary material associated with this article can be found, in the online version, at doi:10.1016/j.actamat.2024.119982.

References

[1] J.A. Halchak, J.L. Cannon, C. Brown, Materials For Liquid Propulsion Systems, American Institute of Aeronautics and Astronautics, 2018.
[2] S. Wolff, Superconducting accelerator magnet design, in: AIP Conf. Proc. (USA), 1992, pp. 1159–1197 (249).

[3] S. Zhao, R. Zhang, Q. Yu, J. Ell, R.O. Ritchie, A.M. Minor, Cryoforged nanotwinned titanium with ultrahigh strength and ductility, Science 373 (6561) (2021) 1363–1368.
[4] C. Ding, H.P. Yun, Mechanical properties of pure titanium and titanium alloys at cryogenic temperatures, Min. Metall. Eng. 22 (3) (2002) 111–114.
[5] Y.M. Wang, E. Ma, R.Z. Valiev, Y.T. Zhu, Tough nanostructured metals at cryogenic temperatures, Adv. Mater. 16 (4) (2004) 328–331.
[6] X.Y. Sun, Y.Z. Guo, Q.M. Wei, Y.L. Li, S.Y. Zhang, A comparative study on the microstructure and mechanical behavior of titanium: ultrafine grain vs. coarse grain, Mater. Sci. Eng. A 669 (2016) 226–245.
[7] M. Zang, H. Niu, J. Yu, H. Zhang, T. Zhang, D. Zhang, Cryogenic tensile properties and deformation behavior of a fine-grained near alpha titanium alloy with an equiaxed microstructure, Mater. Sci. Eng. A 840 (2022) 142952.
[8] Z.W. Huang, D.H. Wen, X.D. Hou, Y.S. Li, B.A. Wang, A.D. Wang, Grain size and temperature mediated twinning ability and strength-ductility correlation in pure titanium, Mater. Sci. Eng. A 849 (2022) 143416.
[9] V.A. Moskalenko, V.I. Startsev, V.N. Kovaleva, Low temperature peculiarities of plastic deformation in titanium and its alloys, Cryogenics (Guildf) 20 (9) (1980) 503–508.
[10] Z.C. Cordero, B.E. Knight, C.A. Schuh, Six decades of the Hall-Petch effect - a survey of grain-size strengthening studies on pure metals, Int. Mater. Rev. 61 (8) (2016) 495–512.
[11] Y.H. Zhao, Y.Z. Guo, Q. Wei, T.D. Topping, A.M. Dangelewicz, Y.T. Zhu, T. G. Langdon, E.J. Lavernia, Influence of specimen dimensions and strain measurement methods on tensile stress-strain curves, Mater. Sci. Eng. A 525 (1–2) (2009) 68–77.
[12] S.V. Zherebtsov, G.S. Dyakonov, A.A. Salem, V.I. Sokolenko, G.A. Salishchev, S. L. Semiatin, Formation of nanostructures in commercial-purity titanium via cryorolling, Acta Mater 61 (4) (2013) 1167–1178.
[13] Y.T. Zhu, X.L. Wu, Ductility and plasticity of nanostructured metals: differences and issues, Mater. Today Nano 2 (2018) 15–20.
[14] A.V. Podolskiy, H.P. Ng, I.A. Psaruk, E.D. Tabachnikova, R. Lapovok, Cryogenic equal channel angular pressing of commercially pure titanium: microstructure and properties, J. Mater. Sci. 49 (19) (2014) 6803–6812.
[15] B.K. Zhao, P. Huang, L.B. Zhang, S.Z. Li, Z. Zhang, Q. Yu, Temperature effect on stacking fault energy and deformation mechanisms in titanium and titanium-aluminium alloy, Sci. Rep. 10 (2020) 3086.
[16] K. Ameyama, F. Cazes, H. Couque, G. Dirras, S. Kikuchi, J. Li, F. Mompiou, K. Mondal, D. Orlov, B. Sharma, D. Tingaud, S.K. Vajpai, Harmonic structure, a promising microstructure design, Mater. Res. Lett. 10 (7) (2022) 440–471.
[17] Y. Zhu, K. Ameyama, P.M. Anderson, I.J. Beyerlein, H. Gao, H.S. Kim, E. Lavernia, S. Mathaudhu, H. Mughrabi, R.O. Ritchie, N. Tsuji, X. Zhang, X. Wu, Heterostructured materials: superior properties from hetero-zone interaction, Mater. Res. Lett. 9 (1) (2021) 1–31.
[18] X.L. Wu, P. Jiang, L. Chen, F.P. Yuan, Y.T.T. Zhu, Extraordinary strain hardening by gradient structure, Proc. Natl. Acad. Sci. U. S. A. 111 (20) (2014) 7197–7201.
[19] Z. Cheng, H.F. Zhou, Q.H. Lu, H.J. Gao, L. Lu, Extra strengthening and work hardening in gradient nanotwinned metals, Science 362 (6414) (2018) 559–566.
[20] X. Li, T. Kreuter, X.M. Luo, R. Schwaiger, G.P. Zhang, Detecting co-deformation behavior of Cu-Au nanolayered composites, Mater. Res. Lett. 5 (1) (2017) 20–28.
[21] C.X. Huang, Y.F. Wang, X.L. Ma, S. Yin, H.W. Hoeppel, M. Goeken, X.L. Wu, H. J. Gao, Y.T. Zhu, Interface affected zone for optimal strength and ductility in heterogeneous laminate, Mater. Today 21 (7) (2018) 713–719.
[22] Q.S. Pan, M.X. Yang, R. Feng, A.C. Chuang, K. An, P.K. Liaw, X.L. Wu, N.R. Tao, L. Lu, Atomic faulting induced exceptional cryogenic strain hardening in gradient cell-structured alloy, Science 382 (6667) (2023) 185–190.
[23] X.L. Ma, C.X. Huang, J. Moering, M. Ruppert, H.W. Hoppel, M. Goken, J. Narayan, Y.T. Zhu, Mechanical properties of copper/bronze laminates: role of interfaces, Acta Mater 116 (2016) 43–52.
[24] X.L. Wu, M.X. Yang, F.P. Yuan, G.L. Wu, Y.J. Wei, X.X. Huang, Y.T. Zhu, Heterogeneous lamella structure unites ultrafine-grain strength with coarse-grain ductility, Proc. Natl. Acad. Sci. U. S. A. 112 (47) (2015) 14501–14505.
[25] Y.T. Zhu, X.L. Wu, Perspective on hetero-deformation induced (HDI) hardening and back stress, Mater. Res. Lett. 7 (10) (2019) 393–398.
[26] Y.T. Zhu, X.L. Wu, Heterostructured materials, Prog. Mater. Sci. 131 (2023) 101019.
[27] R. Wang, M. Wang, R. Jin, Y. Wang, M. Yi, Q. Li, J. Li, K. Zhang, C. Sun, Y. Nie, C. Huang, A.G. Mikos, X. Zhang, High strength titanium with fibrous grain for advanced bone regeneration, Adv. Sci. 10 (16) (2023).
[28] L. Gu, A. Meng, X. Chen, Y.H. Zhao, Simultaneously enhancing strength and ductility of HCP titanium via multi-modal grain induced extra dislocation hardening, Acta Mater 252 (2023) 118949.
[29] M. Ota, S.K. Vajpai, R. Imao, K. Kurokawa, K. Ameyama, Application of high pressure gas jet mill process to fabricate high performance harmonic structure designed pure titanium, Mater. Trans. 56 (1) (2015) 154–159.
[30] M.S. Wang, F.J. Guo, Q. He, W.L. Su, H. Ran, Q. Chen, H.S. Kim, Q.Y. Wang, C. X. Huang, Superior strength-and-ductility synergy by microstructural heterogeneities in pure titanium, Mater. Sci. Eng. A 883 (2023) 145513.
[31] L. Liu, S.F. Li, D. Pan, D.X. Hui, X. Zhang, B. Li, T.S. Liang, P.P. Shi, A. Bahador, J. Umeda, K. Kondoh, S.L. Li, L.A. Gao, Z.M. Wang, G. Li, S.Y. Zhang, R.H. Wang, W.E. Chen, Loss- free tensile ductility of dual- structure titanium composites via an interdiffusion and self- organization strategy, Proc. Natl. Acad. Sci. U. S. A. 120 (28) (2023).
[32] T. Ungar, A. Borbely, The effect of dislocation contrast on x-ray line broadening: a new approach to line profile analysis, Appl. Phys. Lett. 69 (21) (1996) 3173–3175.
[33] H. Wu, M. Huang, Y.P. Xia, X.W. Li, R.E. Li, C.L. Liu, W.M. Gan, T.Q. Xiao, L. Geng, Q. Liu, G.H. Fan, The importance of interfacial stress-affected zone in evading the strength-ductility trade-off of heterogeneous multi-layered composites, Int. J. Plast. (2023) 160.
[34] C.S. Barrett, T.B. Massalski, Structure of Metals: Crystallographic Methods, Principles and Data, Oxford, New York, 1980.
[35] F.J. Humphreys, M. Hatherly, Chapter 12 - Recrystallization Textures, in: F. J. Humphreys, M. Hatherly (Eds.), Recrystallization and Related Annealing Phenomena, (2nd Edition), Elsevier, Oxford, 2004, pp. 67–89, 379-413.
[36] Y.B. Chun, M. Battaini, C.H.J. Davies, S.K. Hwang, Distribution Characteristics of In-Grain Misorientation Axes in Cold-Rolled Commercially Pure Titanium and Their Correlation with Active Slip Modes, Metall. Mater. Trans. A-Phys. Metall. Mater. Sci. 41A (13) (2010) 3473–3487.
[37] C.S.H. EJ, Rapperport Deformation Modes of Zirconium at 77°, 575°, and 1075°K, Trans. Metall. Soc. AIME 218 (1960) 869–876.
[38] Z. Liu, X. Ni, W. Sun, K. Miao, Y. Xia, H. Wu, Z. Wang, G. Fan, Interfacial-constraint-mediated pyramidal slip of hexagonal titanium at room temperature, Scr. Mater. (2022) 221.
[39] M.X. Yang, Y. Pan, F.P. Yuan, Y.T. Zhu, X.L. Wu, Back stress strengthening and strain hardening in gradient structure, Mater. Res. Lett. 4 (3) (2016) 145–151.
[40] Y.H. Zhao, Y.Z. Guo, Q. Wei, A.M. Dangelewicz, C. Xu, Y.T. Zhu, T.G. Langdon, Y. Z. Zhou, E.J. Lavernia, Influence of specimen dimensions on the tensile behavior of ultrafine-grained Cu, Scr. Mater. 59 (6) (2008) 627–630.
[41] Q.Y. Sun, Z.T. Yu, R.H. Zhu, H.C. Gu, Mechanical behavior and deformation mechanisms of Ti-2.5Cu alloy reinforced by nano-scale precipitates at 293 and 77 K, Mater. Sci. Eng. A 364 (1–2) (2004) 159–165.
[42] Q.Y. Sun, H.C. Gu, Tensile and low-cycle fatigue behavior of commercially pure titanium and Ti-5AI-2.5Sn alloy at 293 and 77 K, Mater. Sci. Eng. A 316 (1–2) (2001) 80–86.
[43] D. Boronski, M. Kotyk, P. Mackowiak, L. Sniezek, Mechanical properties of explosively welded AA2519-AA1050-Ti6Al4V layered material at ambient and cryogenic conditions, Mater. Des. 133 (2017) 390–403.
[44] G. Singh, G. Bajargan, R. Datta, U. Ramamurty, Deformation and strength of Ti-6Al-4V alloyed with B at cryogenic temperatures, Mater. Sci. Eng. A 611 (2014) 45–57.
[45] J.W. Christian, S. Mahajan, Deformation twinning, Prog. Mater. Sci. 39 (1–2) (1995) 1–157.
[46] M.A. Meyers, O. Vohringer, V.A. Lubarda, The onset of twinning in metals: a constitutive description, Acta Mater 49 (19) (2001) 4025–4039.
[47] A. Akhtar, Basal slip and twinning in α-titanium single crystals, Metall. Trans. A 6 (5) (1975) 1105–1113.
[48] A. Akhtar, E. Teghtsoonian, Prismatic slip in α-titanium single crystals, Metall. Trans. A 6 (12) (1975) 2201–2208.
[49] H. Gao, Y. Huang, W.D. Nix, J.W. Hutchinson, Mechanism-based strain gradient plasticity— I. Theory, J. Mech. Phys. Solids 47 (6) (1999) 1239–1263.
[50] Y. Huang, H. Gao, W.D. Nix, J.W. Hutchinson, Mechanism-based strain gradient plasticity - II. Analysis, J. Mech. Phys. Solids 48 (1) (2000) 99–128.
[51] C.J. Bayley, W.A.M. Brekelmans, M.G.D. Geers, A comparison of dislocation induced back stress formulations in strain gradient crystal plasticity, Int. J. Solids Struct. 43 (24) (2006) 7268–7286.
[52] J.G. Li, Q. Zhang, R.R. Huang, X.Y. Li, H.J. Gao, Towards understanding the structure-property relationships of heterogeneous-structured materials, Scr. Mater. 186 (2020) 304–311.
[53] Y.F. Wang, Y.T. Zhu, Z.J. Yu, J.F. Zhao, Y.G. Wei, Hetero-zone boundary affected region: a primary microstructural factor controlling extra work hardening in heterostructure, Acta Mater 241 (2022) 118395.
[54] E.O. Hall, The deformation and ageing of mild steel: III discussion of results, Proc. Phys. Soc. Section B 64 (9) (1951) 747.
[55] J.C.M. Li, Y.T. Chou, The role of dislocations in the flow stress grain size relationships, Metall. Trans. 1 (5) (1970) 1145–1159.
[56] R.W. Hertzberg, Richard VinciJason Hertzberg, Deformation and Fracture Mechanics of Engineering Materials, 5th edition, John Wiley & Sons, 2012.
[57] H. Conrad, Effect of interstitial solutes on the strength and ductility of titanium Prog, Mater. Sci. 26 (2–4) (1981) 123–404.
[58] K. Okazaki, H. Conrad, Effects of interstitial content and grain size on the strength of titanium at low temperatures, Acta Metall 21 (8) (1973) 1117–1129.
[59] C. Yin, M. Doner, H. Conrad, The internal stress in titanium deformed at low temperatures ($T<0.33T_m$), Metall. Trans. A 6 (10) (1975) 1901–1908.
[60] H.C.R. Jones, The Science Technology and Application of Titanium, Pergamon Press, New York, 1970.
[61] H. Conrad, Research on mechanical behavior of unalloyed titanium and some selected alloys, Semiannual Report No. 2, U.S. Air Force Contract F33615-68-C-I052 (1969).
[62] H. Conrad, Project Themis "Metal Deformation Processing", Tech. Rept. AFML-TR-71-8 (1971).
[63] E. Clouet, D. Caillard, N. Chaari, F. Onimus, D. Rodney, Dislocation locking versus easy glide in titanium and zirconium, Nat. Mater. 14 (9) (2015) 931–936.
[64] T. Wen, A. Liu, R. Wang, L. Zhang, J. Han, H. Wang, D.J. Srolovitz, Z. Wu, Modelling of dislocations, twins and crack-tips in HCP and BCC Ti, Int. J. Plast. 166 (2023) 103644.
[65] S. Naka, A. Lasalmonie, P. Costa, L.P. Kubin, The low-temperature plastic deformation of α-titanium and the core structure of a-type screw dislocations, Philos. Mag. A 57 (5) (1988) 717–740.